Mon. Not. R. Astron. Soc. **000**, 1–9 (2009) Printed 25 May 2010 (MN LATEX style file v2.2)

arXiv:1005.4399v1 [astro-ph.GA] 24 May 2010

The fragmentation of expanding shells II: Thickness matters.

R. Wünsch[1,2],* J. E. Dale[1], J. Palouš[1] and A. P. Whitworth[2]
[1] *Astronomical Institute, Academy of Sciences of the Czech Republic, Boční II 1401, 141 31 Prague, Czech Republic*
[2] *School of Physics and Astronomy, Cardiff University, Queens Buildings, The Parade, Cardiff, CF24 3AA*

Received:

ABSTRACT

We study analytically the development of gravitational instability in an expanding shell having finite thickness. We consider three models for the radial density profile of the shell: (i) an analytic uniform-density model, (ii) a semi-analytic model obtained by numerical solution of the hydrostatic equilibrium equation, and (iii) a 3D hydrodynamic simulation. We show that all three profiles are in close agreement, and this allows us to use the first model to describe fragments in the radial direction of the shell. We then use non-linear equations describing the time-evolution of a uniform oblate spheroid to derive the growth rates of shell fragments having different sizes. This yields a dispersion relation which depends on the shell thickness, and hence on the pressure confining the shell. We compare this dispersion relation with the dispersion relation obtained using the standard thin-shell analysis, and show that, if the confining pressure is low, only large fragments are unstable. On the other hand, if the confining pressure is high, fragments smaller than predicted by the thin-shell analysis become unstable. Finally, we compare the new dispersion relation with the results of 3D hydrodynamic simulations, and show that the two are in good agreement.

Key words: stars: formation, ISM: HII regions

1 INTRODUCTION

Shells and bubbles are common morphological features in the interstellar media of galaxies, and have been observed at many different wavelengths. For instance, McClure-Griffiths et al. (2002) and Ehlerová & Palouš (2005) have identified ∼ 1000 expanding shells in HI surveys of the Milky Way. HI shells have also been found in the LMC (Kim et al. 1998), the SMC (Hatzidimitriou et al. 2005), and other nearby galaxies. In the infrared, Churchwell et al. (2006, 2007) have assembled a catalogue of ∼ 600 shells found in the GLIMPSE survey of our Galaxy, using the SPITZER space telescope. Shells have been detected in the Wisconsin Hα mapper data (WHAM; Haffner et al. 2003). Shells have also been studied in millimetre molecular line emission, radio continuum and X-rays.

It is generally believed that a substantial fraction of these shells is formed by feedback from massive stars. In addition, it has been suggested by Elmegreen & Lada (1977) that expanding shells can trigger star formation by the *collect-and-collapse* mechanism. In this mechanism, a massive star (or a group of stars) injects energy into the interstellar medium in the form of stellar winds and ionising radiation, and creates a bubble of gas with high temperature. The bubble expands due to its high internal pressure, and sweeps up the ambient medium into a dense shell. The shell cools down, becomes gravitationally unstable, fragments and forms a new generation of stars. If the new generation includes massive stars, the whole process may repeat itself, leading to sequential self-propagating star formation. Various modifications to the collect-and-collapse mechanism are reviewed by Elmegreen (1998).

The collect-and-collapse mechanism has been tested observationally in a series of papers by Deharveng et al. (2003, 2005, 2006, 2008, 2009) and Zavagno et al. (2006). Using data at various wavelengths, they identify and study several objects in which star formation appears to have been triggered at the borders of HII regions. Watson et al. (2008, 2009) analyse six shells from the GLIMPSE survey, and determine the properties of young stellar objects concentrated in these shells.

The gravitational instability of an expanding infinitesimally thin shell has been studied theoretically by several authors. Vishniac (1983) derives a dispersion relation (perturbation growth rate as a function of wavenumber) for an infinitesimally thin shell, using decomposition into spherical harmonics. A very similar dispersion relation is obtained by Elmegreen (1994) using perturbation analysis of linearised two-dimensional hydrodynamic equations. Whitworth et al. (1994) use the equation of motion for a two-dimensional fragment forming on the surface of a shell, and find expressions for the size of the first and most unstable fragment, and for the time at which the instability starts. All these analyses use a very similar physical model (an infinitesimally thin shell which expands into a uniform medium), and although the mathematical description in each of them is very different, the results regarding fragment sizes and growth rates are very similar.

---

* E-mail: richard@wunsch.cz

We have tested these analytic predictions for the growth rate of gravitational instability, based on the thin-shell approximation, in Dale et al. (2009, hereafter Paper I). We use two very different three-dimensional hydrodynamic codes (an Eulerian AMR code and a Lagrangian SPH code) to simulate the evolution and subsequent fragmentation of expanding self-gravitating shells. Our setup differs slightly from the one studied by Vishniac, Elmegreen and Whitworth, in that our shell does not accrete mass from the ambient medium. This modification requires only minor changes to the linear theory of the thin shell gravitational instability, which we describe in §3.1.

We make this modification because an accreting shell is prone to the Vishniac dynamical instability (Vishniac 1983), which would grow quickly and make an analysis of gravitational instability impossible. On the other hand, we want to have the option to keep the shell thin, in order to test the thin-shell approximation. Therefore, we fill the shell interior and exterior with a hot rarefied gas and the pressure of this gas confines the shell. However, because of its low density, the ram pressure of the accreted gas, which is crucial for the development of the Vishniac instability, is negligible. We also keep the pressure of the rarefied gas constant throughout the evolution, so that the shell is effectively in free fall, and development of the Rayleigh-Taylor instability is suppressed.

In Paper I, we find excellent agreement between the two numerical codes. However, for simulations with low confining pressure, in which the shell becomes thick, the simulations do not agree well with the predictions of the thin-shell approximation. The agreement is better for simulations in which the confining pressure is chosen so that the shell thickness stays approximately constant during its evolution.

In this paper (Paper II) we study the gravitational instability of a thick shell analytically, in order to understand how a thick shell fragments, and why the fragmentation differs from the predictions of the thin-shell approximation. We show that the confining pressure, which defines the shell thickness, is an important factor in determining the range of unstable wavelengths. Therefore, we call the new model *pressure assisted gravitational instability* (PAGI).

The outline of the paper is as follows. In §2 we derive a semi-analytic description of the equilibrium radial profile of the shell, and compare it with our 3D numerical simulations, and with the simple uniform-density model of the shell that we adopt in the subsequent analysis. Section §3 deals in detail with modelling gravitational instability in a shell. We briefly derive the dispersion relation for a non-acreting shell, using the thin-shell approximation; we give a description of a fragment forming in a shell with non-zero thickness, and compare it with the description used in the thin-shell approximation; finally we derive a new dispersion relation for a thick pressure-confined shell. In §4, we compare the new dispersion relation with growth rates measured in our 3D numerical simulations, in §5 we discuss the astrophysical consequences of our results, and in §6 we summarise our conclusions.

2 RADIAL DENSITY PROFILE OF THE ISOTHERMAL SHELL

Since we wish to study the influence of the shell's thickness on its gravitational instability, it is essential first to understand the shell's equilibrium radial structure. In Paper I we set the initial radial density profile of the shell using a simple local model for the hydrostatic equilibrium of the gas layer, and assuming that the shell radius is large compared with its thickness:

$$\rho(R) = \rho_{\rm O}\,\mathrm{sech}^2\left[\left(\frac{2\pi G\rho_{\rm O}}{c_{\rm S}^2}\right)^{\frac{1}{2}}(R-R_{\rm O})\right]. \tag{1}$$

Here R is the radial coordinate, $\rho_{\rm O}$ is the maximum density, which appears at the radius $R_{\rm O}$, and $c_{\rm S}$ is the isothermal sound-speed.

A more realistic density profile can be obtained by dropping the assumption that the density profile is symmetric about $R_{\rm O}$ and solving the equation of hydrostatic equilibrium in the form

$$c_{\rm S}^2\frac{d\rho}{dR} = \left\{-\frac{GM(R)}{R^2} + \frac{\alpha GM_{\rm TOT}}{R_\alpha^2}\right\}\rho(R). \tag{2}$$

Here $M(R)$ is the mass within radius R, and α is a dimensionless number between 0 and 1 which has to be found numerically (see below). The first term on the RHS of Eqn. 2 represents the net gravitational acceleration at radius R_α. The second term on the RHS represents the gravitational acceleration of the material at radius R_α, which is the radius that contains a fraction α of the total mass of the shell. This gravitational acceleration is subtracted from the net gravitational acceleration, on the grounds that it contributes to the bulk deceleration of the centre of mass of the expanding shell, rather than its radial profile.

Switching to a Lagrangian formalism (i.e. using M as the independent variable) Eqn. 2 becomes

$$c_{\rm S}^2\left\{\frac{d^2R/dM^2}{(dR/dM)^2} + \frac{2}{R(M)}\right\} = \frac{GM}{R^2(M)} - \frac{\alpha GM_{\rm TOT}}{R_\alpha^2}. \tag{3}$$

Introducing dimensionless variables,

$$\xi = \frac{R}{R_\alpha}, \tag{4}$$

$$\mu = \frac{M(R)}{M_{\rm TOT}}, \tag{5}$$

this reduces to

$$\frac{\xi''}{(\xi')^2} + \frac{2}{\xi} = \frac{GM_{\rm TOT}}{R_\alpha c_{\rm S}^2}\left\{\frac{\mu}{\xi^2} - \alpha\right\}, \tag{6}$$

where $\xi' \equiv d\xi/d\mu$ and $\xi'' \equiv d^2\xi/d\mu^2$.

The shell density profile can be found by solving Eqn. (6) numerically, but we also need to determine the appropriate boundary conditions and the value of α. The shell is confined by the external pressure $P_{\rm EXT}$ on both its inner and outer surfaces, and therefore the density at these surfaces has to be $\rho_{\rm B} = P_{\rm EXT}/c_{\rm S}^2$. Inserting this into the mass conservation law we obtain the inner boundary condition in the form $\left(\xi'\xi^2\right)_{\mu=0} = M_{\rm TOT}c_{\rm S}^2/(4\pi R_\alpha^3 P_{\rm EXT})$. The value $\xi(\mu = 0)$ is unknown, but it can be found by iterating until the boundary condition is also fulfilled at the outer surface, i.e. $\left(\xi'\xi^2\right)_{\mu=1} = M_{\rm TOT}c_{\rm S}^2/(4\pi R_\alpha^3 P_{\rm EXT})$. The parameter α can be found by adding another level of iteration in which α is varied until it fulfils the initial assumption $\xi(\mu = \alpha) = 1$.

Figure 1 compares the radial density profile of the shell in the AMR run from Paper I with $P_{\rm EXT} = 10^{-17}$ dyne cm^{-2}, at time 7.2 Myr, with the semi-analytic profile obtained using Eqn. (6) and the same shell parameters. Both profiles agree very well with each other, which means that the assumption of hydrostatic equilibrium is correct and that the shell is well resolved in the numerical simulation. The time evolution of the shell radius and its FWHM are shown in Figure 2, and this also demonstrates excellent agreement between the numerical and semi-analytic treatments. In §3 we assume that the shell has uniform density with half-thickness given by

$$z_{\rm US} = \frac{\Sigma_{\rm O} c_{\rm S}^2}{2P_{\rm EXT} + \pi G \Sigma_{\rm O}^2} \tag{7}$$

where $\Sigma_{\rm O} \equiv M_{\rm TOT}/(4\pi R_\alpha^2)$ is the shell surface density. This equation is obtained by splitting the shell into two identical layers and then equating the external pressure force and gravitational force acting on one layer due to the other one with the internal pressure force in between the layers. Figures 1 and 2 also display the density profile, mean radius and FWHM of this uniform-density shell model, and show that it is a good approximation to the more detailed models. The agreement between the numerical, semi-analytic and uniform-density models is even better for runs with higher external pressures $P_{\rm EXT} = 10^{-13}$ and $P_{\rm EXT} = 5 \times 10^{-13}$ dyne cm^{-2}.

Figure 2 also shows the evolution of the parameter α. It is close to 0.5 in the beginning of the expansion when the shell is thin and its profile is symmetric, and only decreases by $\sim 10\%$ subsequently. This result supports the assumption of $\alpha = 0.5$ made by Whitworth & Francis (2002).

3 GROWTH RATE OF THE GRAVITATIONAL INSTABILITY

The main aim of this paper is to derive the dispersion relation for gravitational instability of a thick shell, i.e. perturbation growth rate as a function of perturbation wavenumber. For this purpose we model a forming fragment as a uniform-density spheroid whose radial excursions are described by non-linear differential equations. §3.1 briefly summarises the derivation of the thin-shell dispersion relation for the case of a non-accreting shell. §3.2 describes the spheroidal model for a fragment forming in a thick shell, and explains in detail the differences between this model and the model underlying the thin-shell approximation. §3.3 presents the derivation of the PAGI dispersion relation and compares it with the thin-shell dispersion relation.

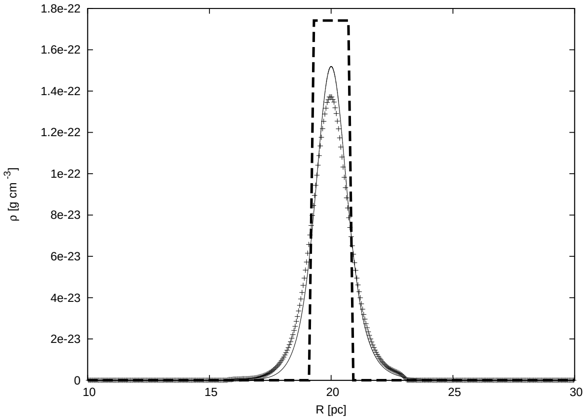

Figure 1. Radial profile of the shell at $t = 7.2$ Myr in 3D AMR simulation (plus symbols), semi-analytical model (solid line) and uniform shell with the same column density (dashed line).

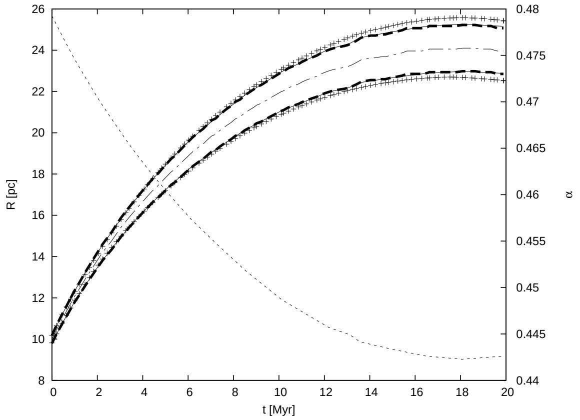

Figure 2. Evolution of the shell FWHM. The dash-dotted line denotes the position of the shell peak density, the other lines below and above it show positions of the the shell inner and outer edge measured at half of the peak density for the three models: 3D AMR simulation (plus symbols), semi-analytical model (thin solid line) and uniform shell (thick dashed line). The thin dashed line shows the evolution of the parameter α.

3.1 Thin shell approximation

Consider an infinitesimally thin shell with radius R and surface density Σ, which expands with velocity V into a vacuum. The shell is isothermal, with sound speed $c_{\rm S}$. The equations describing transverse flows of gas inside the shell are[1].

$$\frac{\partial \Sigma}{\partial t} + R\Sigma\nabla_{\rm T}\cdot\Omega + 2\Sigma\frac{V}{R} = 0\,, \tag{8}$$

$$\Sigma R\frac{\partial \Omega}{\partial t} = -c_{\rm S}^2\nabla_{\rm T}\Sigma - \Sigma\nabla\Phi - \Sigma V\Omega\,, \tag{9}$$

$$\nabla^2\Phi = 4\pi G\Sigma\delta(r - R)\,. \tag{10}$$

Here Ω is the angular velocity of transverse flows, Φ is the gravitational potential, and $\nabla_{\rm T}$ and $\nabla_{\rm T}\cdot$ denote the two-dimensional gradient and divergence, respectively. The instability growth rate is obtained by substituting plane-wave perturbations parametrised by the dimensionless wavenumber $l = kR$ (see Elmegreen 1994, Wünsch & Palouš 2001 and Paper I for details),

---

[1] In Elmegreen (1994) and Wünsch & Palouš (2001) the shell was assumed to accrete mass from the ambient uniform medium, and this resulted in a factor of 4 in front of the last term in the equation of motion, Eqn. 9

$$\begin{aligned} \Sigma &= \Sigma_{\rm O} + \Sigma_l \cos(l\theta)\,, \\ \Omega &= \Omega_l \sin(l\theta)\,, \\ \Phi &= \Phi_{\rm O} + \Phi_l \cos(l\theta)\,. \end{aligned} \tag{11}$$

Here $\Sigma_{\rm O}$ and $\Phi_{\rm O}$ are unperturbed values of the surface density and gravitational potential, Σ_l, Ω_l and Φ_l are the perturbation amplitudes, and θ is an angular coordinate on the surface of the shell in a direction perpendicular to the plane wave. Substituting these perturbations (equation 11) into the linearised equations (8–10), and integrating equation (10) over the thickness of the shell, gives a set of linear differential equations for the amplitudes Σ_l and Ω_l

$$\frac{d}{dt}\begin{pmatrix} \Sigma_l \\ \Omega_l \end{pmatrix} = \begin{pmatrix} -\frac{2V}{R}, & -l\Sigma_{\rm O} \\ \frac{lc_{\rm S}^2}{\Sigma_{\rm O} R^2} - \frac{2\pi G}{R}, & -\frac{V}{R} \end{pmatrix} \begin{pmatrix} \Sigma_l \\ \Omega_l l \end{pmatrix}. \tag{12}$$

The set of equations (12) has two eigenvalues

$$\omega^{(1,2)}_{\rm THIN}(l) = -\frac{3V}{2R} \pm \sqrt{\frac{V^2}{4R^2} + \frac{2\pi G \Sigma_{\rm O} l}{R} - \frac{c_{\rm S}^2 l^2}{R^2}} \tag{13}$$

and two related eigenvectors

$$e^{(1,2)}_l = \begin{pmatrix} -l\Sigma_{\rm O} \\ \omega^{(1,2)} + \frac{2V}{R} \end{pmatrix}. \tag{14}$$

Any harmonic plane-wave perturbation of the shell described by amplitudes Σ_l and Ω_l can be written in the form

$$\begin{pmatrix} \Sigma_l \\ \Omega_l \end{pmatrix} = A e^{(1)}_l + B e^{(2)}_l\,, \tag{15}$$

where A and B are real numbers. Its evolution in the linear regime is then given by

$$\begin{pmatrix} \Sigma \\ \Omega \end{pmatrix} = A e^{(1)}_l \exp(\omega^{(1)} t) + B e^{(2)}_l \exp(\omega^{(2)} t)\,. \tag{16}$$

If a perturbation is given by the eigenvector (2) only (i.e. A = 0), the mode is always damped (since $\omega^{(2)}$ is always negative). On the other hand, if some perturbation is described by eigen-vector (1), it will grow if the gravity term in $\omega^{(1)}$ is large enough.

3.2 Fragment in the thick shell

It turns out that the thin-shell approximation is a good description of the linear instability at wavelengths larger than the shell thickness, provided the shell thickness is uniform. However, in Paper I we find that the shell thickness varies with the surface density of the perturbation, even if its amplitude is relatively small. The spatially varying shell thickness has two effects. (i) In a low-pressure environment, the gas at the centre of a fragment expands in the direction perpendicular to the shell surface, and this results in a slower growth rate and a smaller range of unstable wavelengths, compared with the predictions of the thin-shell approximation. (ii) In a high-pressure environment, the external pressure helps to compress fragments from the side, and this results in a higher growth rate and a larger range of unstable wavelengths, compared with the predictions of the thin-shell approximation.

In order to take the variable thickness of the shell into account, we model a fragment as a uniform-density oblate spheroid with major axis r and minor axis z, embedded in an ambient medium with pressure $P_{\rm EXT}$. Radial excursions of the spheroid are then controlled by the equations of motion

$$\begin{aligned} \ddot{r}(r,z) \;&\simeq\; -\frac{3Gm}{2}\left\{\frac{r\,\cos^{-1}(z/r)}{(r^2-z^2)^{3/2}} - \frac{z/r}{(r^2-z^2)}\right\} \\ &\qquad - \frac{20\pi P_{\rm EXT} r z}{3m} + \frac{5c_{\rm S}^2}{r} \end{aligned} \tag{17}$$

and

$$\begin{aligned} \ddot{z}(r,z) \;&\simeq\; -3Gm\left\{\frac{1}{(r^2-z^2)} - \frac{z\,\cos^{-1}(z/r)}{(r^2-z^2)^{3/2}}\right\} \\ &\qquad - \frac{20\pi P_{\rm EXT} r^2}{3m} + \frac{5c_{\rm S}^2}{z} \end{aligned} \tag{18}$$

(see Boyd & Whitworth 2005).

We assume that the mass of the spheroid, m, is constant, and originates from a comoving circular patch on the shell, with constant angular wavenumber l, and hence radius $\pi R(t)/l$.

The evolution of the spheroid can be followed by solving equations (17) and (18) numerically, as in Boyd & Whitworth (2005). However, in order to derive an analytic dispersion relation for PAGI, we define $t = 0$ as the time when fragmentation starts, and then we assume that for a certain time, t_ϵ, thereafter the spheroid collapses with constant acceleration $\ddot{r}_0$ given by equation (17) with $r = r_0$. Here $r_0 = \pi R/l$ is the initial radius of the fragment, and its initial expansion speed is $\dot{r}_0 = \pi V/l$, where V is the radial velocity of the shell. The subscript ϵ denotes the fraction by which the fragment radius shrinks during t_ϵ (i.e. $r(t_\epsilon) = (1-\epsilon) r_0$). The evolution of the spheroid radius is then given by

$$r(t) = r_0 + \dot{r}_0 t + \frac{1}{2}\ddot{r}_0 t^2\,. \tag{19}$$

and hence t_ϵ is given by

$$\ddot{r}_0 t_\epsilon^2 \,+\, 2\dot{r}_0 t_\epsilon \,+\, 2\epsilon r_0 \;=\; 0\,. \tag{20}$$

In the thin-shell analysis, the instability growth rate is defined as the inverse of the time it takes for the perturbation described by a given eigenvector to grow by a factor e. Since eigenvectors are not available for PAGI, we define the instability growth rate simply as

$$\omega_\epsilon = \frac{1}{t_\epsilon}\,. \tag{21}$$

Since ω_ϵ depends on the choice of ϵ, its absolute value is somewhat arbitrary. However, relative values of ω_ϵ for different wavenumbers are well defined. Moreover, the range of unstable wavenumbers is independent of ϵ and can therefore be compared directly with the range predicted by the thin-shell dispersion relation $\omega_{\rm THIN}$. Combining Eqns. 21 and 20, we obtain the PAGI dispersion relation in the form

$$\omega_\epsilon = -\frac{\dot{r}_0}{2\epsilon r_0} + \sqrt{\left(\frac{\dot{r}_0}{2\epsilon r_0}\right)^2 - \frac{\ddot{r}_0}{2\epsilon r_0}}\,. \tag{22}$$

Figure 3 illustrates the models used in the two analy-

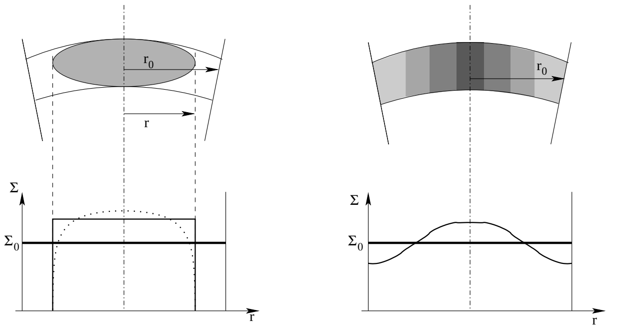

Figure 3. Comparison of fragment models in the thin shell approach (right) and the thick shell approach (left). The approximations are: sine-shaped surface density and velocity perturbation (thin) vs. uniform oblate spheroid (thick); and solution of linearised hydrodynamic equations (thin) vs. constant acceleration coming from non-linear equations of motion (thick).

ses of shell gravitational instability. In the thin-shell analysis, the fragment is modelled as a sine-shaped perturbation of the surface-density and the velocity, on an infinitesimally thin shell. Its growth rate is obtained by solving linearised hydrodynamic equations. In the PAGI analysis, the fragment is modelled as a uniform-density oblate spheroid contained by a constant ambient pressure. It is assumed to contract with constant acceleration given by the non-linear equations of motion evaluated at the onset of instability.

3.3 Dispersion relation of the thick shell

The final form of the dispersion relation is obtained by substituting $m_0 = \pi r_0^2 \Sigma_0$, $r_0 = \pi R_0/l$, $\dot{r}_0 = \pi V_0/l$ (where Σ_0, R_0 and V_0 are – respectively – the surface-density, radius, and radial velocity of the shell when the instability commences), and $\ddot{r}_0 = \ddot{r}(r_0, z_0)$ (Eqn. 17) with $z_0 = \Sigma c_{\rm S}^2 / \left(2P_{\rm EXT} + \pi G \Sigma_0^2\right)$ (Eqn. 7). This yields

$$\begin{aligned}
\omega_\epsilon \;=\; & -\frac{V_0}{2\epsilon R_0} + \left\{ \left(\frac{V_0}{2\epsilon R_0}\right)^2 \right. \\
& + \frac{3\pi G \Sigma_0}{4\epsilon} \left[\frac{r_0^2 \, \cos^{-1}\left(z_0/r_0\right)}{\left(r_0^2 - z_0^2\right)^{3/2}} - \frac{z_0}{\left(r_0^2 - z_0^2\right)} \right] \\
& + \frac{10 P_{\rm EXT} c_{\rm S}^2 l^2}{3\pi^2 \epsilon R_0^2 (2P_{\rm EXT} + \pi G \Sigma_0^2)} \\
& \left. - \frac{5 c_{\rm S}^2 l^2}{2\pi^2 \epsilon R_0^2} \right\}^{1/2} . \qquad (23)
\end{aligned}$$

Equation (23) has a very similar structure to the thin-shell dispersion relation (Eqn. 13), in that the first two terms on the right hand side (line one) represent stretching due to expansion, the third term (line two) represents self-gravity, and the final term (line four) represents internal pressure. However, there are significant differences. (i) The terms all depend on the value of ϵ. We revisit this issue below. (ii) The stretching terms have different numerical coefficients because the initial conditions for the analyses are different. In the thin-shell analysis, the initial perturbation consists of harmonic waves in both surface-density and velocity, given by eigenvectors (Eqn. 14). In the PAGI analysis, the fragment starts life as a uniform-density spheroid expanding with the shell. (iii) The self-gravity term reflects the vertical height of the spheroid, z_0. For a spherical fragment ($z_0 = r_0$), the term in the square bracket is $2/3r_0$. As the fragment becomes flatter, this term increases, and in the limit of an infinitesimally thin fragment ($z_0 = 0$) it becomes $\pi/2r_0$ (an increase of $3\pi/4 \simeq 2.36$). (iv) The fourth term in Eqn. 23 (line three) represents the effect of external pressure, and therefore has no equivalent in Eqn. 13.

Due to the dependence of the absolute value of the PAGI dispersion relation on ϵ it is not possible to compare ω_ϵ to $\omega_{\rm THIN}$ directly (we remind the reader that only the absolute value of ω_ϵ depends on ϵ, the range of unstable wavelengths as well as the relative growth rates of individual modes are ϵ-independent). However, we can define a critical pressure $P_{\rm THIN}$ such that with $P_{\rm EXT} = P_{\rm THIN}$ the range of unstable wavenumbers predicted by the PAGI analysis is the same as that predicted by the thin-shell analysis. Then, for this choice of $P_{\rm EXT}$, we find ϵ for which Eqns. (23) and (13) predict very similar growth rates ($\omega_\epsilon(l, P_{\rm THIN}) \simeq \omega_{\rm THIN}(l)$). This is shown by Figure 4, for the shell from Paper I in two states: the initial radius $R = 10$ pc and the maximum radius $R = 23$ pc. It can be seen that $\omega_\epsilon(l, P_{\rm THIN}) \simeq \omega_{\rm THIN}(l)$ if we set $\epsilon = 0.1$, for both shell radii. Moreover, this value of ϵ results in both dispersion relations being close to each other throughout the whole shell expansion and we therefore adopt this as our default value of ϵ.

Figure 5 compares the PAGI dispersion relation for different values of $P_{\rm EXT}$ with the thin-shell dispersion relation. We have used parameters for a shell having a mass of $2 \times 10^4\,{\rm M}_\odot$, (a) with radius 10 pc and outward radial velocity $2.2\,{\rm km\,s^{-1}}$, and (b) with radius 23 pc and zero outward radial velocity; this is the same as the shell that we simulated in Paper I. Increasing $P_{\rm EXT}$ results in a larger range of unstable wavenumbers, *and* faster growth rates, but even as $P_{\rm EXT} \to \infty$, the maximum unstable wavenumber, $l_{\rm PAGI}^{\rm MAX}$ remains finite. Specifically, for $P_{\rm EXT} = 0$, $l_{\rm PAGI}^{\rm MAX} = 0.595 l_{\rm THIN}^{\rm MAX}$, and for $P_{\rm EXT} = \infty$, $l_{\rm PAGI}^{\rm MAX} = 2.2 l_{\rm THIN}^{\rm MAX}$, where $l_{\rm THIN}^{\rm MAX}$ is the maximum unstable wavenumber according to the thin-shell dispersion relation; evidently an infinitesimally thin shell (i.e. PAGI with $P_{\rm EXT} = \infty$) does not give the same dispersion relation as the thin-shell model.

Figure 6 shows how the ratio $l_{\rm PAGI}^{\rm MAX}/l_{\rm THIN}^{\rm MAX}$ varies with $P_{\rm EXT}$. The vertical line denotes the critical external pressure, $P_{\rm CRIT} = \pi G \Sigma_0^2/2$, at which the derivative of the shell thickness ($z_{\rm US}$) with respect to its surface density (Σ_0) is zero, i.e. the configuration in which external pressure and self gravity make equal contributions to containment of the shell, and the shell thickness is only weakly dependent on its surface-density. This is why $P_{\rm CRIT}$ is approximately equal to $P_{\rm THIN}$ (where $l_{\rm PAGI}^{\rm MAX}/l_{\rm THIN}^{\rm MAX} = 1$). With this external pressure, as a fragment starts to form, and its surface-density increases, its thickness does not change much, and therefore the external pressure force remains largely perpendicular to the surface of the shell and does not make a significant contribution to the lateral squashing of the fragment.

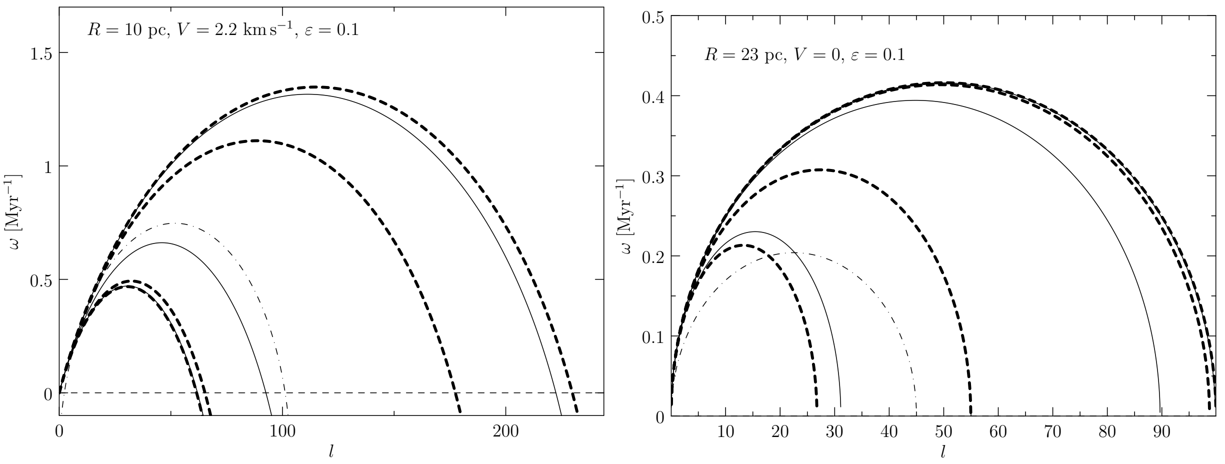

Figure 5. Perturbation growth rate for different values of external pressure for two states of the shell from paper I: $R = 10$ pc, $V = 2.2$ km s^{-1} (left), $R = 23$ pc, $V = 0$ (right). Alternating dashed and solid lines denote ω_ϵ for $P_{\rm EXT} = 0$, 10^{-14}, 10^{-13}, 10^{-12}, 10^{-11}, 10^{-10} and 1 dyne cm^{-2} (in this order for growing range of unstable wavenumbers). The dash-dotted line shows perturbation growth rate of the thin shell $\omega_{\rm THIN}$. The horizontal dashed line at $\omega = 0$ represents the separation between unstable and damping modes.

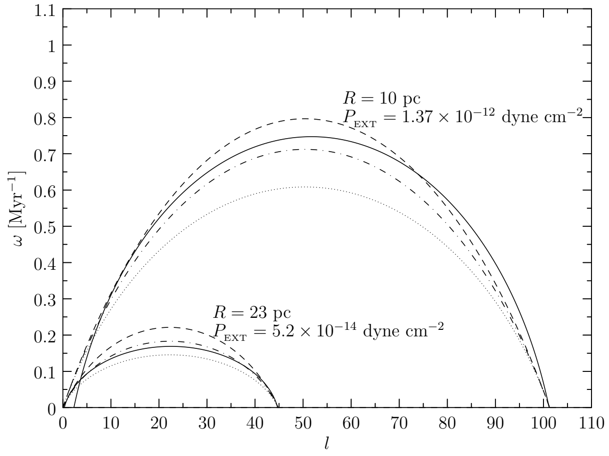

Figure 4. Comparison of the thin shell dispersion relation (Eq. (13), solid lines) and the PAGI dispersion relation (Eq. 23) for three values of ϵ: $\epsilon = 0.05$ (dashed), $\epsilon = 0.1$ (dash-dotted) and $\epsilon = 0.2$ (dotted). Two states of the shell with parameters from Paper I are shown: the initial state ($R = 10$ pc) and the state with the maximum radius $R = 23$ pc. For each state, the external pressure $P_{\rm EXT} = P_{\rm THIN}$ was calculated so that $\omega_{\rm THIN}(l)$ and $\omega_\epsilon(l, P_{\rm THIN})$ give the same range of unstable modes.

4 COMPARISON WITH NUMERICAL SIMULATIONS

In Paper I we have studied numerically the evolution of a shell with mass $M = 2 \times 10^4\,{\rm M}_\odot$, temperature $T = 10$ K, initial radius $R_{\rm ini} = 10$ pc and initial expansion velocity $V_{\rm ini} = 2.2$ km s^{-1}, embedded in a rarefied medium with pressure $P_{\rm EXT}$. After about 18 Myr, the expansion stalls, at radius $R_{\rm max} = 23$ pc, and the shell starts to collapse.

We have run simulations with three different external pressures $P_{\rm EXT} = 10^{-17}$, $P_{\rm EXT} = 10^{-13}$ and $P_{\rm EXT} = 5 \times 10^{-13}$ dyne cm^{-2}; the first one is as close to zero as the hydrodynamic solver permits, the second one is chosen so that the shell thickness varies as little as possible during the shell evolution, and the third one is the highest pressure for which the shell thickness can be resolved with the available computational power.

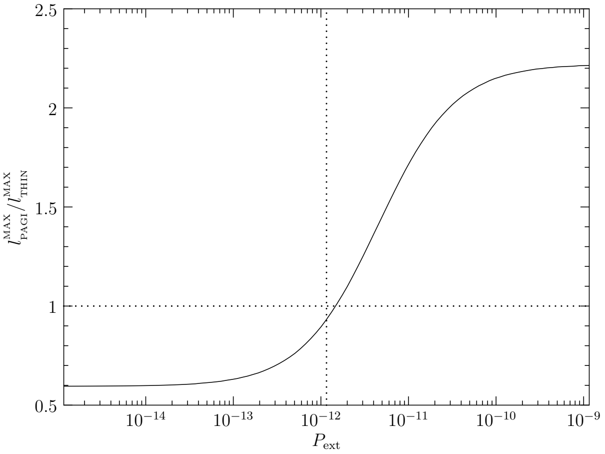

Figure 6. Ratio of the shortest unstable modes given by the thick shell and thin shell models as a function of the external pressure $P_{\rm EXT}$. The vertical dotted line denotes value of $P_{\rm CRIT}$ for which the shell has the maximum thickness for a given surface density.

Figures 7 and 8 summarize results from the hydrodynamic simulations. In the low-pressure run, we find that the perturbation growth rates diverge significantly from the predictions of the thin-shell dispersion relation $\omega_{\rm THIN}(l)$ – only the low wavenumbers grow. The agreement is better for the medium-pressure simulation. The high pressure run again diverges from the predictions given by $\omega_{\rm THIN}(l)$ – the range of unstable modes includes higher wavenumbers than predicted. Differences in relative growth rates among the three simulations result in different fragment sizes as can be seen in figure 8.

The dispersion relation obtained from numerical simulations exhibits several peaks in some cases (see the top middle panel of Figure 7). Among them, only the first peak (at lowest wavenumbers) is suitable for analysis of mode growth rates. The other peaks represent higher harmonics

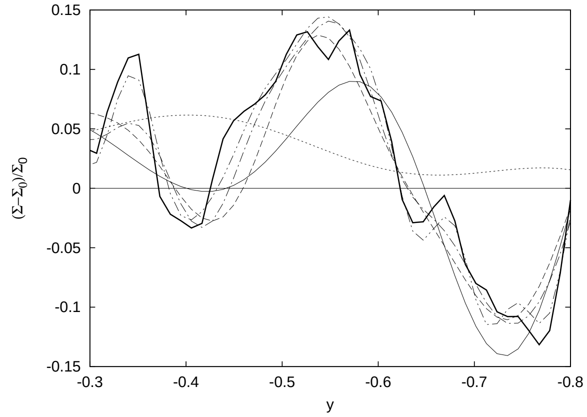

Figure 9. Surface density profile of the fragment from the simulation with $P_{\rm EXT} = 10^{-17}$ dyne cm^{-2} at $t = 15$ Myr (corresponding to the top middle panel of Figure 7 and the left panel of Figure 8). The profile is taken along the Hammer projection coordinate at $x = -0.7$. The thick solid line is the actual surface density in the simulation, the other lines are a sequance of its spherical harmonics representation with modes up to a certain wavenumber: $l < 15$ (dotted), $l < 30$ (thin solid), $l < 45$ (dashed), $l < 60$ (dash-dotted) and $l < 95$ (dash-doubledotted).

of the first peak and their growth is induced by the growth of modes from the first peak. The higher harmonic peaks describe fragment shapes which are typically more concentrated than pure spherical harmonics with wavelengths corresponding to fragment sizes. This is illustrated by Figure 9 which shows the surface density profile across an arbitrary fragment in the simulation with $P_{\rm EXT} = 10^{-17}$ dyne cm^{-2} and a sequence of its representation by spherical harmonics which take into account only modes up to a certain wavenumber. It can be seen that the modes from the first peak only ($l < 30$) are enough to obtain approximately the correct fragment wavelength. If the second peak ($l < 45$) is taken into account the representation of the fragment is already very good. Taking into account modes with $l > 45$ results in further small improvements in representing the detailed shape of the fragment.

The perturbation growth rates from the numerical simulations agree much more closely with the predictions of the PAGI dispersion relation (Eqn. 23). The agreement is best at intermediate times. At earlier times the numerical simulation has not yet had sufficient time to relax and so the modes are poorly defined. At later times the gravitational instability has become strongly non-linear. However, the PAGI dispersion relation does tend to give a slightly larger range of unstable wavenumbers than the numerical simulations.

5 DISCUSSION

The PAGI dispersion relation predicts that the fragment mass function depends on the external pressure confining the shell. Shells expanding into a low pressure environment, for instance shells at higher galactic latitudes, should fragment preferentially on long wavelengths. This may result in a top-heavy core mass function (CMF). However, it remains an open question whether the massive fragments will form massive stars or whether they will continue to fragment into smaller pieces. In the low pressure simulation presented in this work, the large fragments include relatively dense cores (whose growth is represented by distinctive higher harmonics in measured mode growth rates), and the evolution exhibits rather merging of fragment cores than fragment splitting. However, this can be due to our physical model being too simple (isothermal equation of state, relatively small perturbations of initial density and velocity, no radiation, stellar feedback, etc.). To answer this question properly, more realistic simulations would be necessary.

If a top-heavy CMF results in a generation of stars with a top-heavy IMF, this should be favourable to the production of further shells, and hence to sequential self-propagating star formation (Elmegreen & Lada 1977). However, it is a question if such secondary shells expanding into low density gas are able to collect enough mass, cool down and fragment. An example of such a shell in a low density environment might be the Carina Flare super-shell GSH 287+04-17, which extends up to ∼ 450 pc above the galactic plane (Fukui et al. 1999; Dawson et al. 2008).

In Paper I and in this paper, we have studied shells expanding into a hot rarefied gas. Such shells are confined only by their self gravity and by external thermal pressure. This model is applicable to shells which break out of a molecular cloud and expand into a rarefied warm intercloud medium. Our reason for focusing on this model is that we want to study pure gravitational instability. By reducing the density of the ambient gas and hence making its ram pressure negligible, we suppress the typically much faster Vishniac instability.

For a shell expanding into the relatively dense gas of a molecular cloud, ram pressure plays an important role in compressing the outer surface of the shell. The Vishniac instability is then inevitable, because ram pressure acts purely parallel to the direction of shell expansion, whereas thermal pressure acts perpendicular to the surface of the shell. Furthermore, ram pressure cannot compress a fragment laterally, and we therefore expect that in this situation the growth of small fragments would be slower than predicted by the PAGI dispersion relation (Eqn. 23).

The PAGI dispersion relation predicts a range of unstable wavenumbers which is systematically larger by ∼ 25% than the range obtained from numerical simulations. This discrepancy appears at high wavenumbers, so it is unlikely to be due to the curvature of the shell (which is not taken into account in the derivation of ω_ϵ), because the high wavenumbers are least affected by it. The most probable source of this discrepancy is the approximation of spheroid evolution by collapse (or expansion) with constant acceleration (Eq. 19). This is certainly not true, as shown by Boyd & Whitworth (2005), who found complex behaviour for spheroids in the non-linear regime. However, the aim of this work is not to give an accurate description of the fragment evolution, but to obtain an analytical formula which quickly provides information about the instability of a given wavelength on the shell and which takes into account the effects of external pressure.

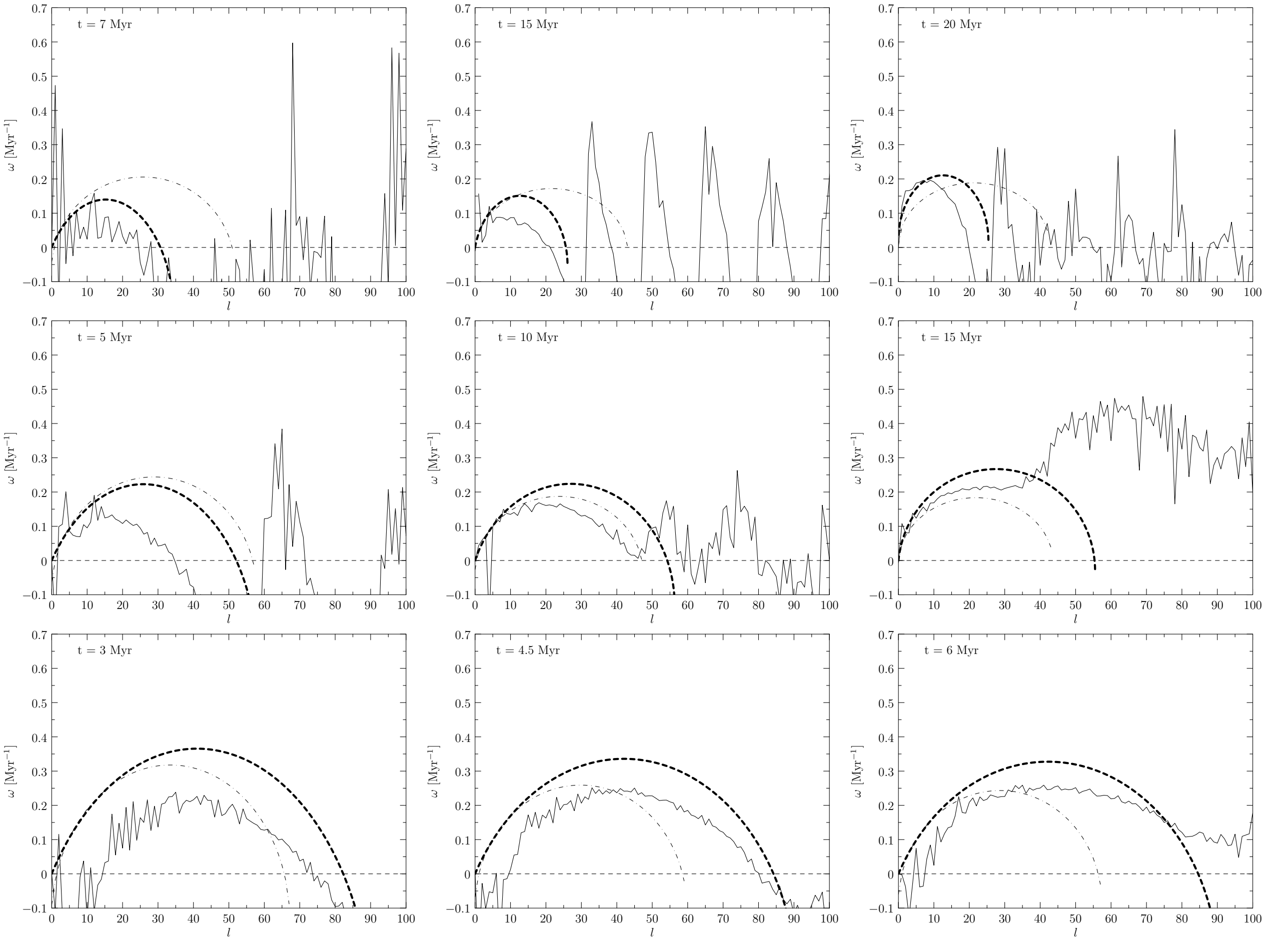

Figure 7. The perturbation growth rate in hydrodynamic simulations, compared to both the thin-shell and the PAGI dispersion relations. The top panels show the simulation with $P_{\rm EXT} = 10^{-17}\,{\rm dyne\,cm^{-2}}$; the middle panels show the simulation with $P_{\rm EXT} = 10^{-13}\,{\rm dyne\,cm^{-2}}$; and the bottom panels show the simulation with $P_{\rm EXT} = 5 \times 10^{-13}\,{\rm dyne\,cm^{-2}}$. In all panels only the first (approximately parabolic) peak at low wavenumbers should be compared with the analysis. The other peaks are higher harmonics, which reflect the shapes adopted by fragments in the non-linear condensation regime. The horizontal dashed line at $\omega = 0$ represents the separation between unstable and damping modes.

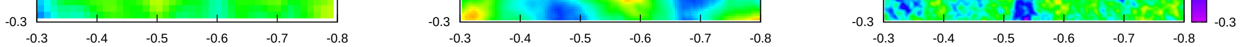

Figure 8. Normalised surface density ($\Sigma/\Sigma_{\rm O}$) for the three hydrodynamic simulations with different external pressures: $P_{\rm EXT} = 10^{-17}$ (left), $P_{\rm EXT} = 10^{-13}$ (middle) and $P_{\rm EXT} = 5 \times 10^{-13}$ dyne cm^{-2} (right). Panels show a randomly chosen part of the shell surface of the size 0.4×0.4 radians (the axes are denoted in Hammer projection coordinates). The times are the same as for the middle column of the figure 7, i.e. 15, 10 and 4.5 Myr for the low, medium and high pressure simulation, respectively.

6 CONCLUSIONS

We have studied an isothermal ballistic shell, confined from both sides by a hot highly rarefied gas having non-zero pressure, $P_{\rm EXT}$. We have solved the equation of hydrostatic equilibrium in a frame of reference moving with the shell and shown that the resulting shell density profiles are in very good agreement with the profiles obtained from three-dimensional hydrodynamic simulations. We have also shown that the shell thickness measured at half of its peak density agrees well with the thickness of a simple uniform-density shell model.

This allows us to model a fragment forming in the shell, due to gravitational instability, as a uniform-density oblate spheroid. We use this model to derive a dispersion relation for pressure assisted gravitational instability (PAGI). This dispersion relation (perturbation growth rate as a function of initial fragment wavenumber) depends on the pressure of the external medium: the higher $P_{\rm EXT}$, the larger the maximum unstable wavenumber (i.e. the smaller the smallest unstable fragment), and the faster the growth rate for an unstable fragment. If $P_{\rm EXT} = 0$, the highest unstable wavenumber is 0.6 times smaller than predicted by the standard thin-shell analysis using the same parameters; if $P_{\rm EXT} = \infty$, the highest unstable wavenumber is 2.2 times larger. The PAGI dispersion relation gives approximately the same range of unstable wavelengths as the thin-shell dispersion relation if $P_{\rm EXT} \simeq P_{\rm CRIT}$, where $P_{\rm CRIT}$ is the critical external pressure for which self-gravity and external pressure contribute equally to confinement of the shell.

Finally, we have demonstrated that the predictions of the PAGI dispersion relation agree rather well with the results of three-dimensional hydrodynamic simulations. In particular, (i) the PAGI dispersion relation predicts a maximum unstable wavenumber very similar to the simulations (but systematically $\sim 25\%$ higher); (ii) modulo this offset, the increase in $l_{\rm PAGI}^{\rm MAX}$ with $P_{\rm EXT}$ predicted by the PAGI dispersion relation is exactly mirrored by the simulations.

7 ACKNOWLEDGMENTS

The authors thank the anonymous referee for his/her very thorough reading of the paper and constructive comments. The FLASH code was developed in part by the DOE-supported Alliances Center for Astrophysical Thermonuclear Flashes at the University of Chicago. The AMR calculations were performed on the Cardiff University HPC Cluster MERLIN. The SPH simulations were performed on the Virgo cluster of the Astronomical Institute of the Academy of Science of the Czech Republic, v. v. i. RW acknowledges support by the Human Resources and Mobility Programme of the European Community under contract MEIF-CT-2006-039802. JED acknowledges support from a Marie Curie fellowship as part of the European Commission FP6 Research Training Network 'CONSTELLATION' under contract MRTN–CT–2006–035890. JED, RW and JP acknowledge support from the Institutional Research Plan AV0Z10030501 of the Academy of Sciences of the Czech Republic and project LC06014–Centre for Theoretical Astrophysics of the Ministry of Education, Youth and Sports of the Czech Republic. APW acknowledges the support of STFC grant PP/E000967/1.

REFERENCES

Boyd D. F. A., Whitworth A. P., 2005, A&A, 430, 1059

Churchwell E., Povich M. S., Allen D., Taylor M. G., Meade M. R., Babler B. L., Indebetouw R., Watson C., Whitney B. A., Wolfire M. G., Bania T. M., Benjamin R. A., Clemens D. P., Cohen M., Cyganowski C. J., Jackson J. M., Kobulnicky H. A., Mathis J. S., 2006, ApJ, 649, 759

Churchwell E., Watson D. F., Povich M. S., Taylor M. G., Babler B. L., Meade M. R., Benjamin R. A., Indebetouw R., Whitney B. A., 2007, ApJ, 670, 428

Dale J. E., Wünsch R., Whitworth A., Palouš J., 2009, MNRAS, 398, 1537

Dawson J. R., Kawamura A., Mizuno N., Onishi T., Fukui Y., 2008, PASJ, 60, 1297

Deharveng L., Lefloch B., Kurtz S., Nadeau D., Pomarès M., Caplan J., Zavagno A., 2008, A&A, 482, 585

Deharveng L., Lefloch B., Massi F., Brand J., Kurtz S., Zavagno A., Caplan J., 2006, A&A, 458, 191

Deharveng L., Lefloch B., Zavagno A., Caplan J., Whitworth A. P., Nadeau D., Martín S., 2003, A&A, 408, L25

Deharveng L., Zavagno A., Caplan J., 2005, A&A, 433, 565

Deharveng L., Zavagno A., Schuller F., Caplan J., Pomarès M., De Breuck C., 2009, A&A, 496, 177

Ehlerová S., Palouš J., 2005, A&A, 437, 101

Elmegreen B. G., 1994, ApJ, 427, 384

Elmegreen B. G., 1998, in C. E. Woodward, J. M. Shull, & H. A. Thronson Jr. ed., Origins Vol. 148 of Astronomical Society of the Pacific Conference Series, Observations and Theory of Dynamical Triggers for Star Formation. pp 150–+

Elmegreen B. G., Lada C. J., 1977, ApJ, 214, 725

Fukui Y., Onishi T., Abe R., Kawamura A., Tachihara K., Yamaguchi R., Mizuno A., Ogawa H., 1999, PASJ, 51, 751

Haffner L. M., Reynolds R. J., Tufte S. L., Madsen G. J., Jaehnig K. P., Percival J. W., 2003, ApJS, 149, 405

Hatzidimitriou D., Stanimirovic S., Maragoudaki F., Staveley-Smith L., Dapergolas A., Bratsolis E., 2005, MNRAS, 360, 1171

Kim S., Staveley-Smith L., Dopita M. A., Freeman K. C., Sault R. J., Kesteven M. J., McConnell D., 1998, ApJ, 503, 674

McClure-Griffiths N. M., Dickey J. M., Gaensler B. M., Green A. J., 2002, ApJ, 578, 176

Vishniac E. T., 1983, ApJ, 274, 152

Watson C., Corn T., Churchwell E. B., Babler B. L., Povich M. S., Meade M. R., Whitney B. A., 2009, ApJ, 694, 546

Watson C., Povich M. S., Churchwell E. B., Babler B. L., Chunev G., Hoare M., Indebetouw R., Meade M. R., Robitaille T. P., Whitney B. A., 2008, ApJ, 681, 1341

Whitworth A. P., Bhattal A. S., Chapman S. J., Disney M. J., Turner J. A., 1994, MNRAS, 268, 291

Whitworth A. P., Francis N., 2002, MNRAS, 329, 641

Wünsch R., Palouš J., 2001, A&A, 374, 746

Zavagno A., Deharveng L., Comerón F., Brand J., Massi F., Caplan J., Russeil D., 2006, A&A, 446, 171